JGR Oceans

RESEARCH ARTICLE
10.1029/2022JC019530

Southern Ocean Acidification Revealed by Biogeochemical-Argo Floats

Matthew R. Mazloff[1], Ariane Verdy[1], Sarah T. Gille[1], Kenneth S. Johnson[2], Bruce D. Cornuelle[1], and Jorge Sarmiento[3]

[1]Scripps Institution of Oceanography, University of California San Diego, La Jolla, CA, USA, [2]Monterey Bay Aquarium Research Institute, Moss Landing, CA, USA, [3]Princeton University, Princeton, NJ, USA

Key Points:

- We present a novel 12-month Southern Ocean pH mapped product, made possible by the Biogeochemical-Argo array initiated in 2014
- Comparing to ship-based measurements above 1,500 m reveals a decrease in pH of up to 0.02 per decade
- pH changes are widespread with varying magnitudes reflecting the pattern of the meridional overturning circulation

Supporting Information:

Supporting Information may be found in the online version of this article.

Correspondence to:

M. R. Mazloff,
mmazloff@ucsd.edu

Citation:

Mazloff, M. R., Verdy, A., Gille, S. T., Johnson, K. S., Cornuelle, B. D., & Sarmiento, J. (2023). Southern Ocean acidification revealed by biogeochemical-Argo floats. *Journal of Geophysical Research: Oceans*, *128*, e2022JC019530. https://doi.org/10.1029/2022JC019530

Received 1 DEC 2022
Accepted 2 MAY 2023

Abstract Ocean acidification has potentially large impacts on calcifying organisms and ecosystems. Argo floats equipped with biogeochemical (BGC) sensors have been continuously measuring Southern Ocean pH since 2014. These BGC-Argo floats were deployed as part of the Southern Ocean Carbon and Climate Observations and Modeling project. Here we present a **S**OCCOM-era **O**bjectively **M**apped pH (SOM-pH) 2014–2019 climatology and explain the method for constructing this product. We show example SOM-pH fields demonstrating the spatial and temporal structure of Southern Ocean pH. Comparison with previous ship-based measurements reveals decreases in pH of up to 0.02 per decade, with a structure decaying with depth. An assessment of the trend structure reveals a pattern indicative of the meridional overturning circulation. Upwelling waters that have not been in recent contact with the atmosphere show negligible or small trends, while surface and downwelling waters that have had more exposure to the atmosphere show the strongest trends. Thus comparison of this new BGC-Argo mapped pH estimate to historic observations allows quantifying the structure of Southern Ocean acidification.

Plain Language Summary Robotic instruments that measure ocean acidity levels (pH) have been deployed in the Southern Ocean since 2014. Here we compile these observations into a map that is an estimate of the current Southern Ocean pH. This paper discusses how the map is made and gives a brief description of its features. We then compare it to pH measurements made from ships prior to 2014. Analyzing the structure of these differences in space and time reveals how the Southern Ocean is becoming more acidic. We find that there is significant structure to the changes. In general the changes are largest at the surface and become smaller at greater depth. However, there are horizontal differences. Ocean locations where winds pull up deep waters have smaller trends than regions where the winds are pushing waters down. Thus the ocean changes show a signature associated with the large-scale circulation.

1. Introduction

The Southern Ocean is a region of intense air–sea exchange, with regions where mixed layers can reach hundreds of meters deep. Here the abyssal ocean is ventilated, and surface waters are subducted downward to be sequestered away from the atmosphere for centuries (Wunsch & Heimbach, 2008). As such, understanding the carbon cycling of the Southern Ocean is vital. Toward this aim, since 2014 the Southern Ocean Carbon and Climate Observations and Modeling (SOCCOM) project has been deploying robotic biogeochemical profilers, known as BGC-Argo floats. These floats measure pH, O_2, NO_3 and optical properties in addition to temperature, salinity, and pressure (K. S. Johnson et al., 2017). In this paper we focus first on determining the present day pH properties of the Southern Ocean by merging float observations with model analyses, and second on assessing how the properties have changed in time.

Our primary goal is reporting pH trend magnitudes. This is important as ocean acidification (i.e., decreasing oceanic pH and lowering calcium carbonate saturation state) can have large impacts on calcifying organisms (Doney et al., 2009, 2020; Henley et al., 2020). These organisms struggle to build skeletons and shells in low pH waters where aragonite becomes undersaturated. The impacts of this stress can propagate across the Antarctic ecosystems and further. While it is pressing to address this issue globally, it is especially important to quantify Southern Ocean pH, as acidification is hypothesized to be occurring faster here than in the global average due to the region's relatively low carbonate ion concentrations (McNeil & Matear, 2008; Orr et al., 2005).

Decline in upper ocean pH has been observed throughout the Southern Ocean (Takahashi et al., 2014), with trend values around −0.02 per decade in Drake Passage (Munro et al., 2015) and in the South Pacific (Midorikawa et al., 2012; Williams et al., 2015). Regional differences are found. For example, a larger trend was found poleward of the Polar Front (PF) than equatorward, and was attributed to intensified wind-driven upwelling of deep carbon-rich waters (Midorikawa et al., 2012). Uptake of atmospheric CO_2 and oceanic advection of anthropogenic carbon also contributed to the observed acidification (Henley et al., 2020).

Our secondary goal is to determine the spatial pattern of the trend, and pose hypotheses for causal mechanisms based on this pattern. We investigate the relationship of trend magnitude with known water masses and circulation patterns. The Southern Ocean can be categorized by spatial regions (Gray et al., 2018; Orsi et al., 1995; Talley, 2011). The most poleward region is often referred to as the Sea Ice Zone (SIZ). The Antarctic Circumpolar Current (ACC) system is found north of the SIZ, with the region between the Southern ACC Front (SACCF; ranging from 54.0° to 65.5°S with a mean of 59.8°S) and the Polar Front (PF; ranging from 46.5° to 61.9°S with a mean of 54.4°S) known as the Antarctic Zone (AZ). Moving equatorward, but still in the ACC, the Polar Frontal Zone (PFZ) sits between the PF and the Subantarctic Front (SAF; ranging from 38.3° to 57.9°S with a mean of 49.7°S). To the north of the ACC the Subantarctic Zone (SAZ) is found between the SAF and the Subtropical Front (STF; ranging from 33.4° to 48.1°S with a mean of 42.3°S). The Subtropical Zone (STZ) is the most equatorward zone found in the Southern Ocean. The circulation is broadly characterized by upwelling of Upper and Lower Circumpolar Deep Water (UCDW, LCDW) in the AZ. Upwelled waters then travel both poleward and equatorward, interact with the atmosphere, and subduct again to form a double cell Meridional Overturning Circulation (MOC, Marshall & Speer, 2012). The poleward traveling waters become Antarctic Surface Waters (AASW) and eventually subduct as Antarctic Bottom Waters (AABW) to form the lower MOC cell. Equatorward traveling waters are transformed into Subantarctic Mode Water (SAMW), Antarctic Intermediate Water (AAIW), and Subantarctic Surface Water (SASW), and populate the upper MOC cell. We aim to assess how pH changes project on these zones and water masses.

In addition to BGC-Argo floats there are two resources enabling this work. The first is bias corrected monthly mean fields from a Biogeochemical Southern Ocean State Estimate (B-SOSE, Verdy & Mazloff, 2017). The bias correction is determined by objectively mapping the monthly binned BGC-Argo pH measurement differences to B-SOSE. This correction field is then added to the B-SOSE monthly means to determine a **S**OCCOM-era **O**bjectively **M**apped pH (SOM-pH) product. By construction, the derived product has much of the same structure as B-SOSE, but with negligible bias compared to the BGC-Argo pH observations from which it is created. SOM-pH is a monthly, spatially smooth, pH mapped estimate that is intended to average out eddy signals, making it ideal for comparison to historical observations. This stands in contrast to previous match-up-based comparison methods used to infer changes (Midorikawa et al., 2012; Ríos et al., 2015; Swart et al., 2018), as smoothing the eddy signals can reduce the noise incurred in match-ups.

The other resource allowing us to estimate pH trends and patterns are the quality controlled in situ pH measurements from the Global Ocean Data Analysis Project version 2 (GLODAPv2) data set. These GLODAPv2 data, the BGC-Argo float data, and B-SOSE are described in Section 2. The methods used in the work, including the algorithm for constructing the SOM-pH product, are described in Section 3. In Section 4 the GLODAPv2 and SOM-pH differences are cataloged by depth and region, and linear regressions are applied with respect to time to determine trends. We find significant trends, with a spatial structure indicative of the influence of the Southern Ocean MOC, and we end with a discussion of this result in Section 5.

2. Data

Throughout this analysis, total scale pH at in situ temperature and pressure is used for all products.

2.1. GLODAPv2

GLODAPv2 is a synthesis of biogeochemical data collected through chemical analysis of water samples. Discrepancies in observational methodologies do result in uncertainties (Carter et al., 2018; Liu et al., 2011; Yao et al., 2007), but the data has been subjected to quality control to identify outliers and correct for most measurement biases (Key et al., 2015; Olsen et al., 2016). The 2019 release includes pH observations taken between 1994 and 2017 (Olsen et al., 2019). However, these are concentrated around the summer season and along repeat

hydrography lines. These data are largely independent from the mapped climatology presented here, the caveat being that they were used to develop B-SOSE. GLODAPv2 also provides a gridded product normalized to the year 2002 (Lauvset et al., 2016), to which we compare in the results section.

2.2. BGC-Argo

Argo profiling floats are providing temperature and salinity measurements of the global ocean (G. C. Johnson et al., 2022). Since 2014, some of these floats have been equipped with biogeochemical sensors and deployed through the SOCCOM project (Riser et al., 2018). The BGC-Argo-derived pH data that are used for our mapping were obtained from the Argo Global Data Assembly Centre (Argo GDAC) on 30 March 2021 (Argo, 2020). Details on the pH measurements and quality control can be found in K. S. Johnson et al. (2017) and Maurer et al. (2021). Briefly, pH was measured with Deep-Sea DuraFET sensors (K. S. Johnson et al., 2016) that quantify proton activity with an Ion Sensitive Field Effect Transistor. Each sensor was calibrated in the laboratory to determine its temperature and pressure response. The sensor reference potential was calibrated for pH on the total proton scale using spectrophotometric pH measured with purified meta-cresol purple (Liu et al., 2011). After deployment, sensors were corrected for drift or offsets in the reference potential using the SOCCOM Assessment and Graphical Evaluation (SAGE) software (Maurer et al., 2021). SAGE assesses statistically significant drift or offset by comparing sensor measurements at depths below 1,000 m to values predicted from empirical models fit to ship-based measurements (Bittig et al., 2018; Carter et al., 2018) and driven by float oxygen, temperature, salinity, and position data.

2.3. B-SOSE

B-SOSE assimilates satellite and in situ physical and biogeochemical data, including both GLODAPv2 and BGC-Argo data, into the MIT ocean general circulation model using the software developed by the consortium for Estimating the Circulation and Climate of the Ocean (ECCO, Wunsch & Heimbach, 2013). The biogeochemical component is known as the Nitrogen version of the Biogeochemistry with Light, Iron, Nutrients, and Gases model (NBLING, evolved from Galbraith et al., 2010). NBLING includes a full accounting for budgets of carbon, oxygen, nitrate, phosphate, and iron. Three phytoplankton classes are also modeled.

The B-SOSE objective is to estimate the large-scale Southern Ocean biogeochemical and physical properties, including sea ice, and provide complete budget-closing diagnostics enabling interpretation of this evolving state. The aim is to be as consistent as possible with observations. To accomplish this the assimilation procedure adjusts model inputs of initial conditions and atmospheric state. However, due to the closed-budget model constraint there is no nudging of interior ocean properties, and thus B-SOSE may exhibit biases with respect to the assimilated data.

The first B-SOSE produced was a solution with 1/3° grid spacing for the period 2008–2012. Validation, analysis, model inputs, code, and comprehensive diagnostics have been published demonstrating the maturity of BGC state estimation (Verdy & Mazloff, 2017). A subsequent 2013–2019 SOCCOM-era B-SOSE was produced at 1/6° grid spacing. This work uses the "Iteration 135" of this 1/6° B-SOSE solution (available at http://sose.ucsd.edu/SO6/ITER135/).

3. Methods

3.1. Construction of a pH 2014–2019 Climatology

The SOM-pH product is constructed with a remove/restore objective mapping procedure to bias correct B-SOSE. The remove step involves calculating the B-SOSE–observation misfits. These misfits are objectively mapped to make a bias correction field. The restore step involves adding the bias correction field to B-SOSE. To start we take the "Iteration 135" B-SOSE solution and make monthly averages of potential temperature (T), salinity (S), and pH sampled point by point on a $1° \times 1°$ horizontal grid at 41 depth levels between 1 and 2,000 m. These fields become the first guess, $\mathbf{x_b}$ (i.e., the background state). This state consists of T, S, and pH. To combine them into one vectorized state space we first remove the time means from the three fields and normalize each by its standard deviation. The BGC-Argo pH and Argo T and S profiles are also vectorized and then normalized in the same way using the model-derived mean and standard deviation values.

B-SOSE assimilates BGC-Argo observations including pH, but still has biases with respect to the observations. The goal is to take this B-SOSE first guess estimate, $\mathbf{x_b}$, and add a monthly bias correction. We define the Argo and BGC-Argo observations as vector $\mathbf{y}$ and define $\mathbf{H}$ to be a 3D trilinear interpolation operator mapping the B-SOSE estimate to data locations. Thus the vector $(\mathbf{y} - \mathbf{Hx_b})$ gives the observation–B-SOSE misfits. We then carry out an objective mapping (also known as optimal interpolation) of these misfits to yield bias correction fields (Bretherton et al., 1976; Ide et al., 1997). Adding these fields back to B-SOSE yields the SOM-pH product, and is derived with the following algorithm,

$$\mathbf{x_a} = \mathbf{x_b} + \left(\mathbf{PH^T}\right)\left(\mathbf{HPH^T} + \mathbf{R}\right)^{-1}(\mathbf{y} - \mathbf{Hx_b}). \quad (1)$$

Here $\mathbf{x_a}$, which is referred to as the "analysis state," is the SOM-pH product. $\mathbf{R}$ is the prescribed "noise" in the data, accounting for all signals not accounted for in the mapping, which includes mesoscale variability. $\mathbf{P}$ is the covariance in space of each variable, and also the cross-covariance of the T, S, and pH fields with the other variables. We estimate this full covariance matrix from an ensemble drawn from B-SOSE, but damp the cross-covariance of pH with T and S by a factor of 0.1, because T and S observations far outnumber pH observations, and we want the mapping to lean more heavily on the pH observations.

We also damp spurious long-distance covariance by applying a "localization" operator that reduces the covariance magnitude between distant points. This damping is set using a Gaspari and Cohn (1999) localization function with scales of 21° longitude, 7° latitude, and 2 "vertical levels." Vertical level spacing increases with depth. The mapping algorithm can be influenced by observations at up to twice these distances depending on $\mathbf{P}$, but this influence is downweighted as a function of distance.

In the method $\mathbf{PH^T}$ represents our estimate of the covariance of the quantity to be estimated (i.e., pH) and the data, the model–data covariance matrix. Similarly $(\mathbf{HPH^T + R})$ represents our estimate of the covariance between all pairs of data, the so-called data–data covariance matrix. Thus we first project the data–B-SOSE differences through the inverse of the data–data covariance in order to account for data redundancy and mutual-information, and then project the result onto the model grid via the model–data covariance matrix. As the data–data covariance matrix functions as the denominator of this equation, the influence of the data decreases as $\mathbf{R}$ increases.

The choice of the signal-to-noise ratio, roughly the magnitude of $\mathbf{P}$ compared to the magnitude of $\mathbf{R}$, has a significant impact on the solution. Here, we have normalized the data, so the signal covariance, $\mathbf{P}$, has a magnitude of approximately 1, making the signal-to-noise determined by $\mathbf{R}$. As stated above, $\mathbf{R}$ accounts for all signals unaccounted for in the mapping. For pH we choose $\mathbf{R}$ to be the spatially variable uncertainty used in B-SOSE (Verdy & Mazloff, 2017), which was derived from a model-variability analysis (i.e., it is a specified fraction of the standard deviation of a long free model run), though normalized in consistency with the data. To emphasize the use of pH observations in construction of the map, we use a much larger value of $\mathbf{R} = 100$ for temperature and salinity.

We generate a bias-corrected map for each month. There are a few mapped points that end up appearing questionable or unphysical, likely due to large variability in the data that is not properly accounted for in the setup of the problem (e.g., a poor choice of signal to noise). Therefore, once the 12 monthly maps are constructed, we carry out a quality control process by comparing monthly map values to the adjacent months. No temporal correlation was assumed during the mapping process, so this is an independent quality control opportunity to alleviate the impact of data outliers. For each grid point and for each month, we calculate the absolute difference with the previous and the next months (pH_{t-1} and pH_{t+1}, respectively). Values are replaced with the average between pH_{t-1} and pH_{t+1} if they meet the following criteria: (a) both differences exceed a threshold; (b) the value is an extremum of the time series; and (c) pH_{t-1} and pH_{t+1} do not meet criteria 1 and 2. This is applied twice, the first time with a threshold value of 5 times the pH uncertainty field, $\mathbf{R}$, used in the mapping, and the second time with a threshold value of 2 times $\mathbf{R}$. This QC procedure results in replacement of approximately 1% of grid points, implying we are not throwing out important signals.

3.2. Outlier Removal and Trend Fitting Methods for Comparison of SOM-pH to Historic Data

To achieve our goal of examining trend magnitudes and spatial patterns, the historic data differences from SOM-pH are sorted in spatial bins. Here we discuss two methods employed in the analysis. The first is an outlier removal for each bin, and the second involves calculating the trends and their uncertainty. We are fitting trends in sparse data, and this section describes of how the uncertainty calculation accounts for this temporal spread.

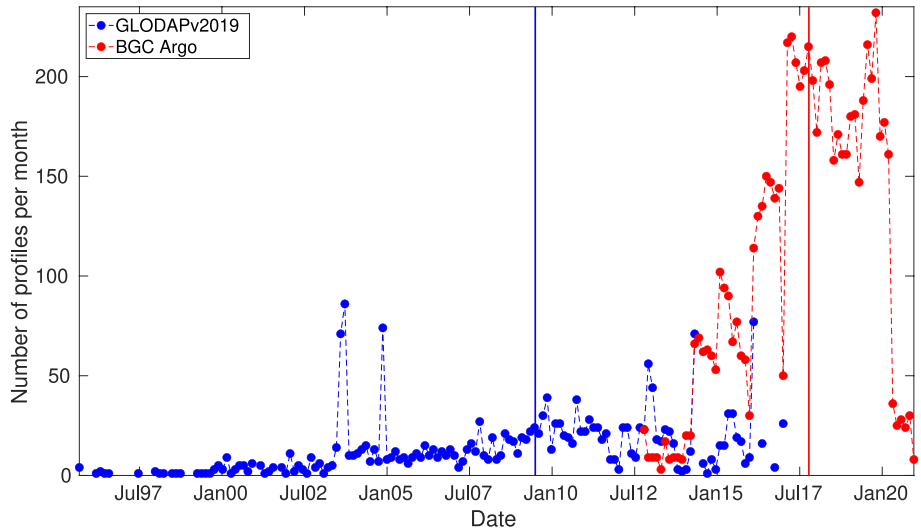

Figure 1. Number of profiles for a given month, with Global Ocean Data Analysis Project version 2 (GLODAPv2) in blue and BGC-Argo in red. The vertical blue line gives the mean date of the GLODAPv2 observations, which is June 2009. The mean data of the BGC-Argo observations used (vertical red line) is October 2017. A minimal amount of BGC-Argo data from 2013 to 2020 are used in the Southern Ocean Carbon and Climate Observations and Modeling-era Objectively Mapped pH product, and thus we consider it a 2014–2019 product in the text.

In each spatial bin we take the difference of the GLODAPv2 observations with SOM-pH, and we find that there are occasional large differences (i.e., outliers). These are likely real signals due to eddy variability, but due to sparse sampling could be overly influential. In an attempt to evaluate the influence of outliers on the trend values, we analyze the misfits over 1-month periods and remove observations that exceed 2 standard deviations. The following plots are made with the outliers removed, but this stringent outlier removal has only a small effect. The results for plots with and without outliers are similar (not shown), giving us confidence that outliers are not impacting our results.

To solve for trends in each spatial bin the differences between the GLODAPv2 observations and SOM-pH are written as a vector, $\mathbf{y}$. Each difference is assigned an assumed uncertainty of $r = 0.01$. These differences occur at discrete times, and we define $\mathbf{H}$ as the regression matrix with the first column being the observation time. The trend we seek is given by $x(1)$, where we solve for this slope $x(1)$, as well as an intercept, $x(2)$, given the equality $\mathbf{y} = \mathbf{Hx} + \mathbf{r}$. Here $\mathbf{r}$ is a vector of values given by r^2. Also, since $x(2)$ is the intercept a second column of $\mathbf{H}$ exists that is all ones.

Unlike the data-space inversion used to make the SOM-pH map presented in Section 3.1, here we solve in parameter space with the solution being $\mathbf{x} = \left(\mathbf{H}^T\mathbf{R}^{-1}\mathbf{H} + \mathbf{P}^{-1}\right)^{-1}\ \mathbf{H}^T\mathbf{R}^{-1}\ \mathbf{y}$ (Wunsch, 2006). Here $\mathbf{R}$ is the data uncertainty with values of r^2 on the diagonal, and P(1,1) is the expected trend uncertainty on the slope $x(1)$ that we have assigned to be 0.01 per decade. The uncertainty we report is given by the square root of the first diagonal element of $\left(\mathbf{H}^T\mathbf{R}^{-1}\mathbf{H} + \mathbf{P}^{-1}\right)^{-1}$. The uncertainty is thus reduced by more data or wider temporal coverage, both represented in the $\mathbf{H}$ matrix, or by lower data uncertainty, which is represented in the $\mathbf{R}$ matrix.

4. Results

4.1. The SOM-pH Product

The SOM-pH is constructed using the monthly binned Argo and BGC-Argo data. The pH data count as a function of time is shown in Figure 1, which shows that the SOM-pH product represents a mean of approximately 2014–2019, with a "center of mass" of October 2017 (i.e., the SOCCOM-era, though the data are continuing to stream in, and we anticipate updated products). The full derived SOM-pH product is available as Data Set S1. Here we provide example plots for February and August at 55 and 700 m (Figure 2). Comparing these panels allows evaluation of spatial and temporal gradients. The strongest gradients occur with depth, as the pH at 55 m is much higher than 700 m. There are significant gradients in latitude at both depths, with the pH tending to be

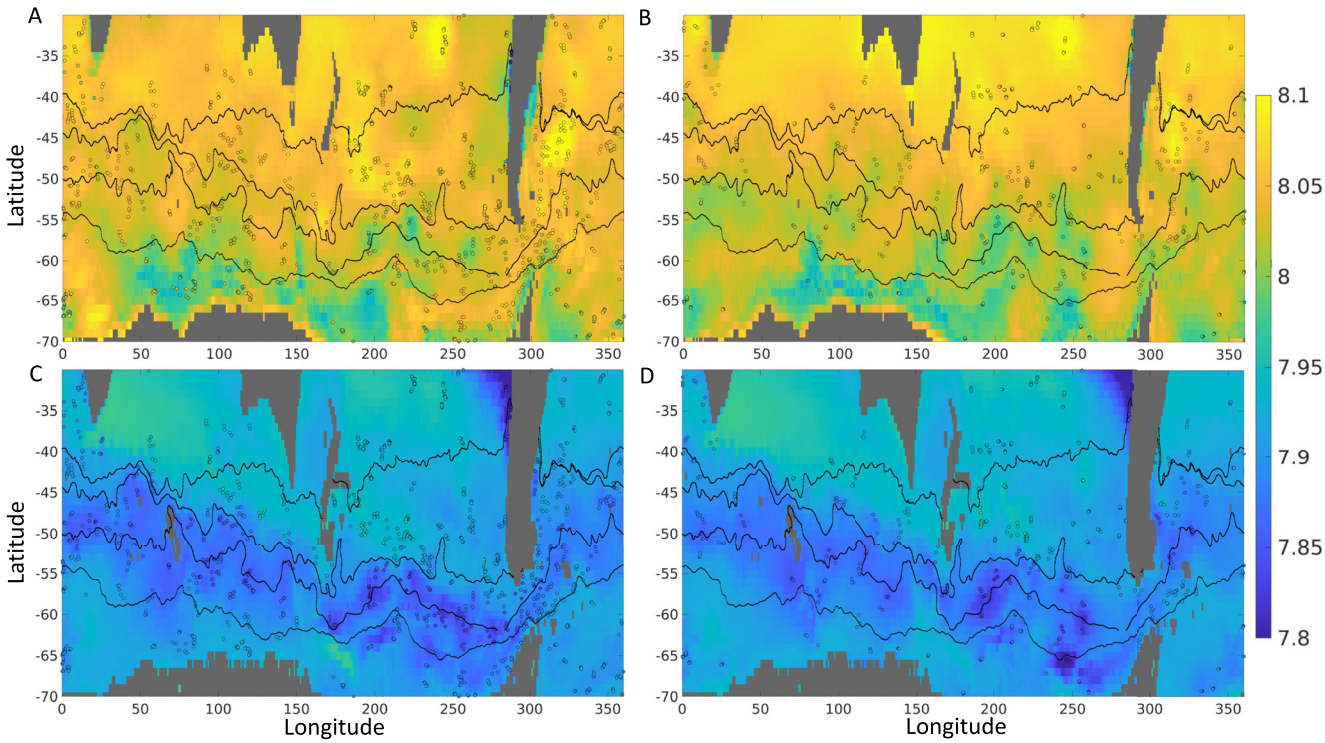

Figure 2. Example pH fields from the Southern Ocean Carbon and Climate Observations and Modeling-era Objectively Mapped pH product: (a) pH at 55 m in February, (b) pH at 55 m in August, (c) pH at 700 m in February, and (d) pH at 700 m in August. BGC-Argo float pH observations are superimposed as filled markers with black outlines, using the same color scale as the background, so that good agreement blends in and mismatches stick out. Black contours denote, from south to north, the Southern ACC Front, Polar Front, Subantarctic Front, and Subtropical Front, following Gray et al. (2018) who used the criteria of Orsi et al. (1995) and an Argo temperature and salinity climatology (Roemmich & Gilson, 2009).

much lower in subpolar waters than in subtropical waters. Strong gradients are also noticeable in other frontal regions and in boundary regions. There is a seasonal cycle, though the gradients in time are not as strong as in space. Even though 55 m tends to be in the mixed layer in winter but not in summer, the pH is not drastically different between February and August.

The pH maps plotted in Figure 2 show the float observations for these depths and months as filled circles. Because some of the mapping information is propagated via the covariance in depth and cross-covariance from temperature and salinity, this is not all the information going into the map. However, it represents the primary constraints. Expanses of the Southern Ocean lack float observations, and in these regions the map relies largely on B-SOSE. To better illustrate the mapping method and the biases that one may expect, we show the differences being mapped and the map itself in Figure 3. Here the circles represent the difference between observations and B-SOSE, and the background color plotted represents the bias correction applied to B-SOSE (i.e., the map). Where there are data, the bias correction is effective at increasing consistency; the original B-SOSE differences and the mapped differences for these example plots are summarized in Table 1. The mean bias in the SOM-pH product is greatly reduced compared to B-SOSE, and the standard deviation of the differences is also diminished.

While the misfit to the float data is significantly smaller in SOM-pH than in B-SOSE for all depths and months, there is a significant caveat. The corrections shown in Figure 3 have large-scale structure; the field does not look noisy. It is apparent that B-SOSE is biased high (i.e., the correction is negative) in the ACC region at 700 m. Though one can infer a large-scale bias, we are not bias correcting far from any pH data. We attempted to bias correct the B-SOSE solution itself by adjusting initial conditions with a constant along isopycnals, but the bias still remains at this point. We also attempted to map using longer correlation scales (i.e., reducing the localization). However, there are eddy signals in the data that then overly influence the maps. Thus gaps with no B-SOSE bias correction exist in the SOM-pH product. Other depths and months show both large-scale residual features and gaps like those in Figure 3 as well. Not all white space in the plots are not gaps in coverage: some represent

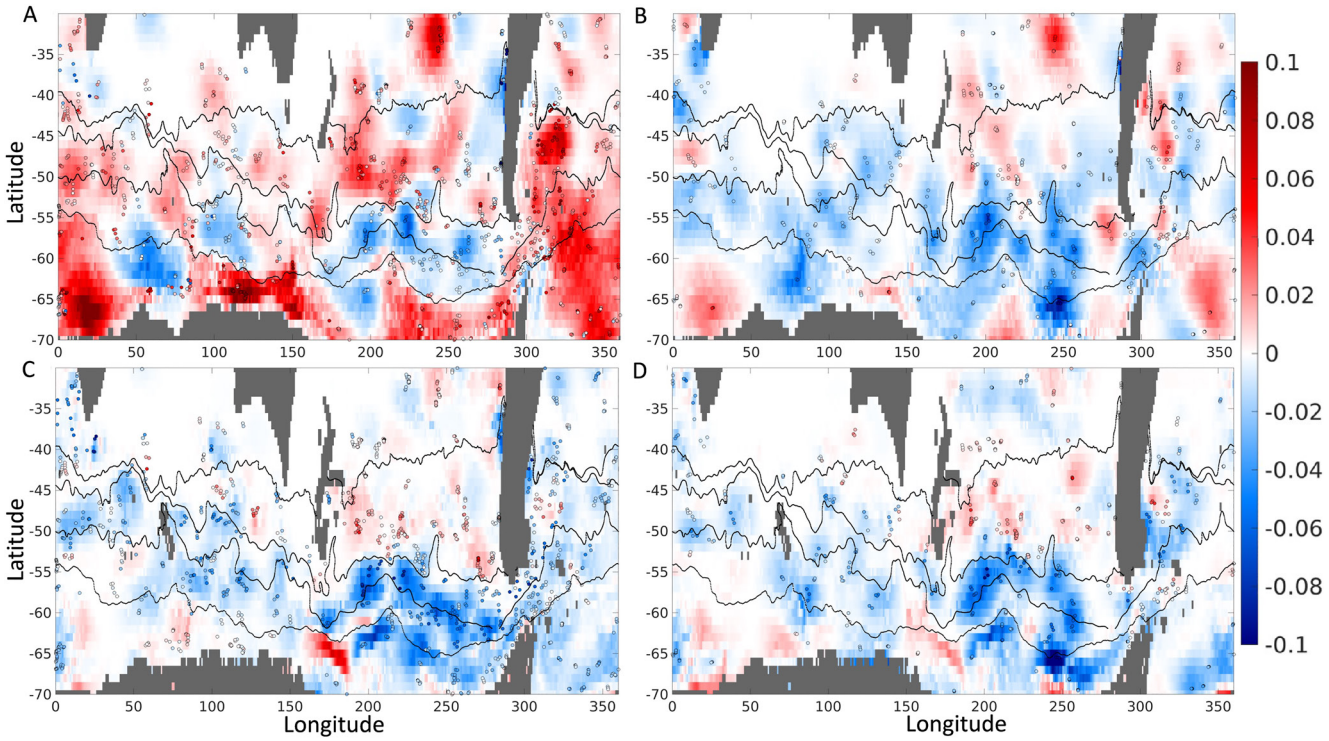

Figure 3. Example bias correction fields. The filled markers represent BGC-Argo differences from B-SOSE. The mapping algorithm spreads this signal in space in accordance with covariance statistics derived from B-SOSE. The bias field derived is then added back to B-SOSE to generate the Southern Ocean Carbon and Climate Observations and Modeling-era Objectively Mapped pH product. Panels show the bias correction fields used in generating the panels in Figure 2. Thus the correction fields are for (a) 55 m in February, (b) 55 m in August, (c) 700 m in February, and (d) 700 m in August. Black contours denote, from south to north, the Southern ACC Front, Polar Front, Subantarctic Front, and Subtropical Front.

regions with minimal B-SOSE bias, while some are in fact coverage gaps. One may infer that in regions away from the float observations the SOM-pH product may still have significant biases relative to the present-day true ocean state. Users should be aware of this uncertainty structure, and a best practice would be to consider the product to have large uncertainty in regions lacking BGC-Argo data coverage over this period.

4.2. Comparison of the SOM-pH Product to the GLODAPv2 Mapped Estimate

The GLODAPv2 release included a mapped pH estimate (Lauvset et al., 2016). This was based on historic ship-based observations and has a bias toward summer observations. In deriving this gridded product the GLODAPv2 data are normalized to 2002, and thus the map represents a period 15 years prior to the SOCCOM mean date. We compare SOM-pH to the GLODAPv2 mapped product at 55 and 700 m, and choose to compare only to the SOM-pH December to March fields due to the GLODAPv2 sampling bias. Figures 4a and 4c are analogous to Figures 2a and 2c, but for the GLODAPv2 map. Also, note that the color axis is different in Panel

Table 1
Example Mean and Standard Deviation (Std) of Differences From the Observations for the Biogeochemical Southern Ocean State Estimate and the Southern Ocean Carbon and Climate Observations and Modeling-Era Objectively Mapped pH Product

	February 55 m		August 55 m		February 700 m		August 700 m	
Product	Mean	Std	Mean	Std	Mean	Std	Mean	Std
B-SOSE	0.017	0.033	−0.007	0.024	−0.014	0.025	−0.016	0.029
SOM-pH	0.002	0.015	0.001	0.008	−0.003	0.012	−0.003	0.013

Note. Differences have been significantly reduced by the mapping.

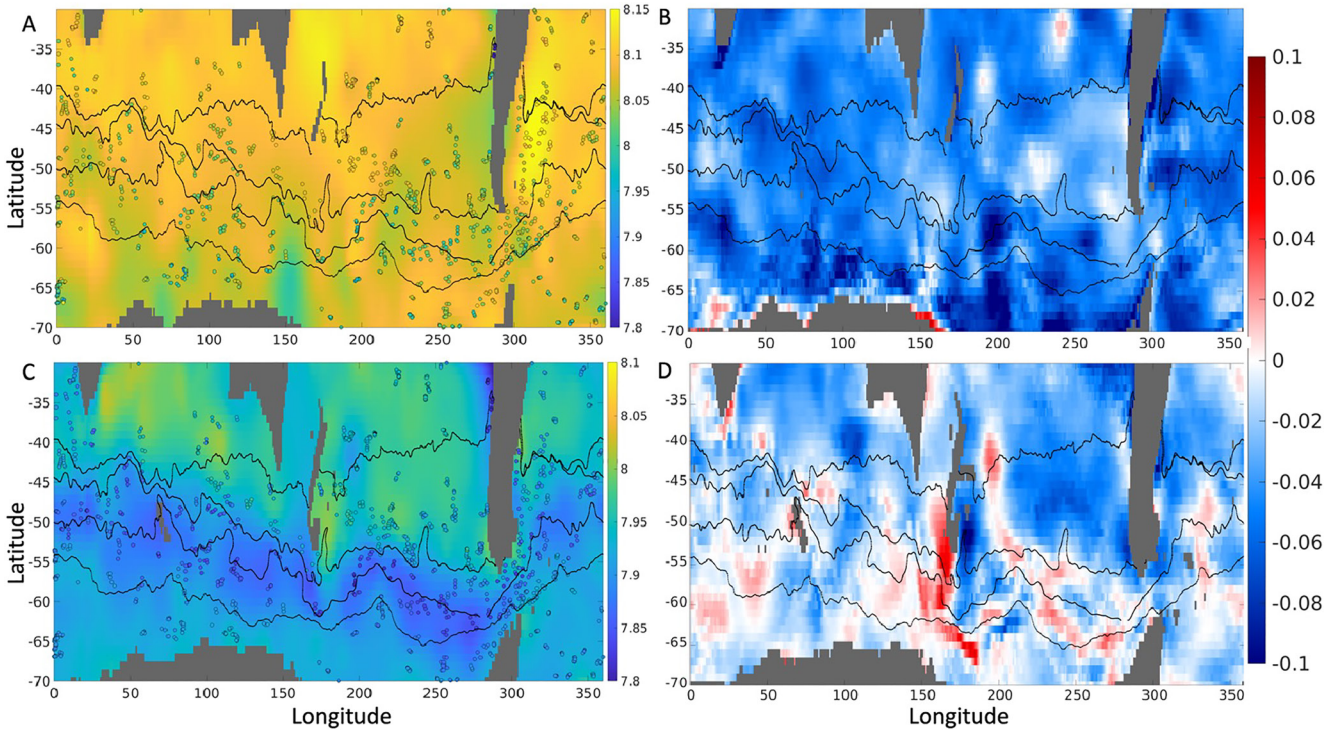

Figure 4. Example pH fields from the Global Ocean Data Analysis Project version 2 (GLODAPv2) mapped product: (a) pH at 55 m and (c) pH at 700 m. These panels are analogous to the Southern Ocean Carbon and Climate Observations and Modeling-era Objectively Mapped pH (SOM-pH) maps shown in Figures 2a and 2c, though the color axes are different in panel (a) as the GLODAPV2 product has much higher pH values. The summer (December to March) BGC-Argo float pH observations are superimposed as filled markers with black outlines. Panel (b) is the difference SOM-pH minus GLODAPv2 at 55 m while Panel (d) is the difference at 700 m. The summer average SOM-pH fields are used for differencing as the GLODAPv2 mapped observations tend to have a summer bias. Black contours denote, from south to north, the Southern ACC Front, Polar Front, Subantarctic Front, and Subtropical Front.

(a), as the GLODAPv2 values are significantly higher than SOM-pH due to the approximately 15 years time difference that the products represent. This difference of SOM-pH minus GLODAPv2 (Figures 4b and 4d) makes it clear that at 55 m the structures are similar, but there is a strong mean difference of up to about 0.1 pH units in the products. At 700 m depth there is also a strong difference reaching about 0.1 pH units in the subtropics, but the difference is patchy in the ACC region and in the subpolar gyres.

The SOM-pH in December to March minus the GLODAPv2 product has a mean at 55 m of −0.049 with a standard deviation of 0.055, and at 700 m the mean difference is −0.019 with a standard deviation of 0.021. Thus there is a clear difference between the GLODAPv2 product made from data taken between 1944 and 2017, and normalized to 2002, and the SOCCOM-era observations representing approximately 2017. In the next section we compare SOM-pH to the raw GLODAPv2 data to assess this change.

4.3. Comparison of SOM-pH to Historic Data

We begin our comparison by sorting the data into five depth bins (100–210, 210–425, 425–750, 750–1,050, and 1,050–1,500 m) and five spatial regions following Gray et al. (2018) who used the criteria of (Orsi et al., 1995) and an Argo temperature and salinity climatology (Roemmich & Gilson, 2009). We assume that the spatial region frontal domains are constant with depth. Figure 5 shows these regions, and also shows the 500 m SOM-pH map, BGC-Argo observations, and GLODAPv2 observations taken prior to 2009. In Figure 5b the differences to SOM-pH are shown, and though at a slightly different depth than the differences shown in Figure 4, they reveal similar magnitudes and structures.

We difference all sorted GLODAPv2 pH observations poleward of 35°S. As explained in the methods Section 3.2, difference outliers in the bins are removed and then a trend and an associated uncertainty are calculated. A significant trend is found in each depth bin, with a magnitude that decreases with depth (Figure 6a). These trend

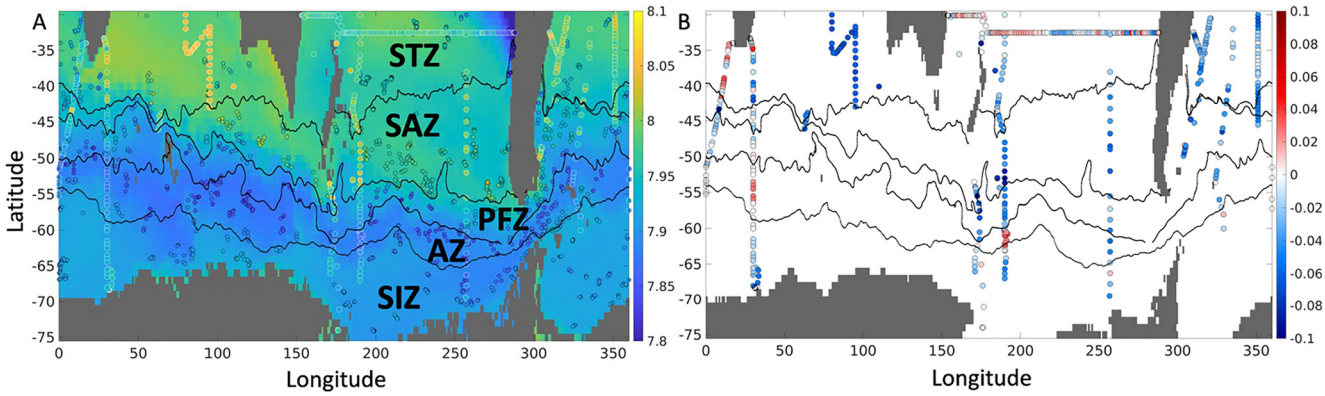

Figure 5. (a) Summer (December to March) average pH from the Southern Ocean Carbon and Climate Observations and Modeling (SOCCOM)-era Objectively Mapped pH (SOM-pH) product at 500 m. The spatial zones of analysis are separated with black contours. From north to south the zones are the Subtropical Zone (STZ), Subantarctic Zone (SAZ), Polar Frontal Zone (PFZ), Antarctic Zone (AZ), and Sea-Ice Zone (SIZ). Small circles with black outlines are 500 m summertime BGC-Argo observations. Larger circles with white outlines are 500 m observations from the Global Ocean Data Analysis Project version 2 (GLODAPv2) database taken prior to 2009, and thus represent the first half of the historical record. This is done to emphasize the change from times before 2009 to the SOCCOM-era of approximately 2017. (b) The summer SOM-pH map minus the GLODAPv2 observations taken prior to 2009 at 500 m. The change is mostly negative indicating reduced pH for the current day state.

values are given in row 1 of Table 2. Next we take the 425–750 m bin and further subdivide the data by spatial domain (Figure 6b). The uncertainties, given in Table 2, show that all trends are significantly different from zero. The overall trend in this depth layer is shown for reference in blue, and the trend is strongest in the PFZ (Figure 6b). The trend in the STZ is greater than the regional average, the SAZ trend matches this regional average, the trend is weaker in the SIZ, and is almost negligible in the AZ.

The average SOM-pH value in each depth bin and region gives the current estimated state, with lower pH at depth and highest pH in the STZ surface waters (Figure 7). Panel C shows this estimate is informed from approximately 3,000 BGC-Argo observations in each depth bin, with roughly 900 in the SIZ and 500 in each of the other four zones. We carry out the trend calculation for both H^+ and pH, as these can be different (Fassbender et al., 2021). However for this analysis we find the results to be qualitatively similar.

In addition to confirming the vertical structure shown in Figure 6a, Figure 7d also demonstrates that the trends display a meridional structure. The largest trends are at the surface in the SIZ and the 210–425 m layer of the SAZ.

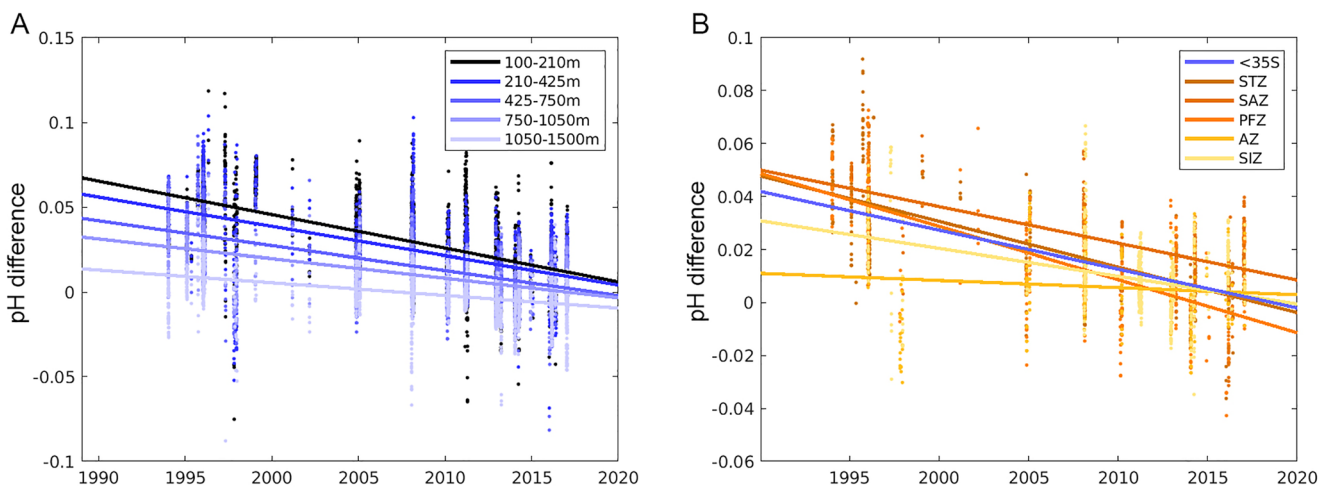

Figure 6. Difference scatter plots and trend fits: Global Ocean Data Analysis Project version 2 observations minus Southern Ocean Carbon and Climate Observations and Modeling-era Objectively Mapped pH (SOM-pH). (a) All observations poleward of 35°S minus SOM-pH binned by depth levels. The colored dots represent individual observations, with most profiles covering all depths such the dots overlay each other. The lines are linear fits. (b) Same as (a), except now binning the 425–750 m bin into each spatial zone. The blue line shows the trend for all observations poleward of 35°S for reference, and thus matches the line for this depth bin in panel (a). An uncertainty analysis deems all trends to be significantly different from zero, with magnitudes and uncertainties presented in Table 2.

Table 2
pH Trend Values and Uncertainty (decade^{-1}) for Each Region and Depth

	100–210 m	210–425 m	425–750 m	750–1,050 m	1,050–1,500 m
<35°S	−0.0199 ± 0.0003	−0.0174 ± 0.0003	−0.0151 ± 0.0003	−0.0114 ± 0.0003	−0.0075 ± 0.0004
STZ	−0.0187 ± 0.0007	−0.0166 ± 0.0006	−0.0170 ± 0.0006	−0.0159 ± 0.0006	−0.0121 ± 0.0007
SAZ	−0.0222 ± 0.0007	−0.0233 ± 0.0006	−0.0142 ± 0.0007	−0.0092 ± 0.0007	−0.0069 ± 0.0007
PFZ	−0.0216 ± 0.0008	−0.0208 ± 0.0008	−0.0207 ± 0.0008	−0.0103 ± 0.0008	−0.0076 ± 0.0009
AZ	−0.0134 ± 0.0010	−0.0023 ± 0.0010	−0.0033 ± 0.0010	0.0002 ± 0.0011	−0.0047 ± 0.0011
SIZ	−0.0242 ± 0.0007	−0.0198 ± 0.0007	−0.0114 ± 0.0008	−0.0091 ± 0.0010	−0.0069 ± 0.0011

Meanwhile the trends in the AZ at 750–1,050 m are indistinguishable from zero. This pattern is indicative of the MOC. We summarize this by superimposing the classic Southern Ocean MOC (Speer et al., 2000; Talley, 2011) on top of the trend plot (Figure 8). Here we can see that where the Upper and Lower Circumpolar Deep Water (UCDW, LCDW) upwells (i.e., in the AZ) the trend is small or negligible. These are old waters and have had the least recent exposure to the surface. Antarctic Surface Water (AASW) sits at the surface of the SIZ and is exposed to the atmosphere. These waters have the strongest pH trend in the Southern Ocean. The upwelling UCDW and some LCDW interact with the atmosphere and other upper ocean water masses to be transformed into SAMW,

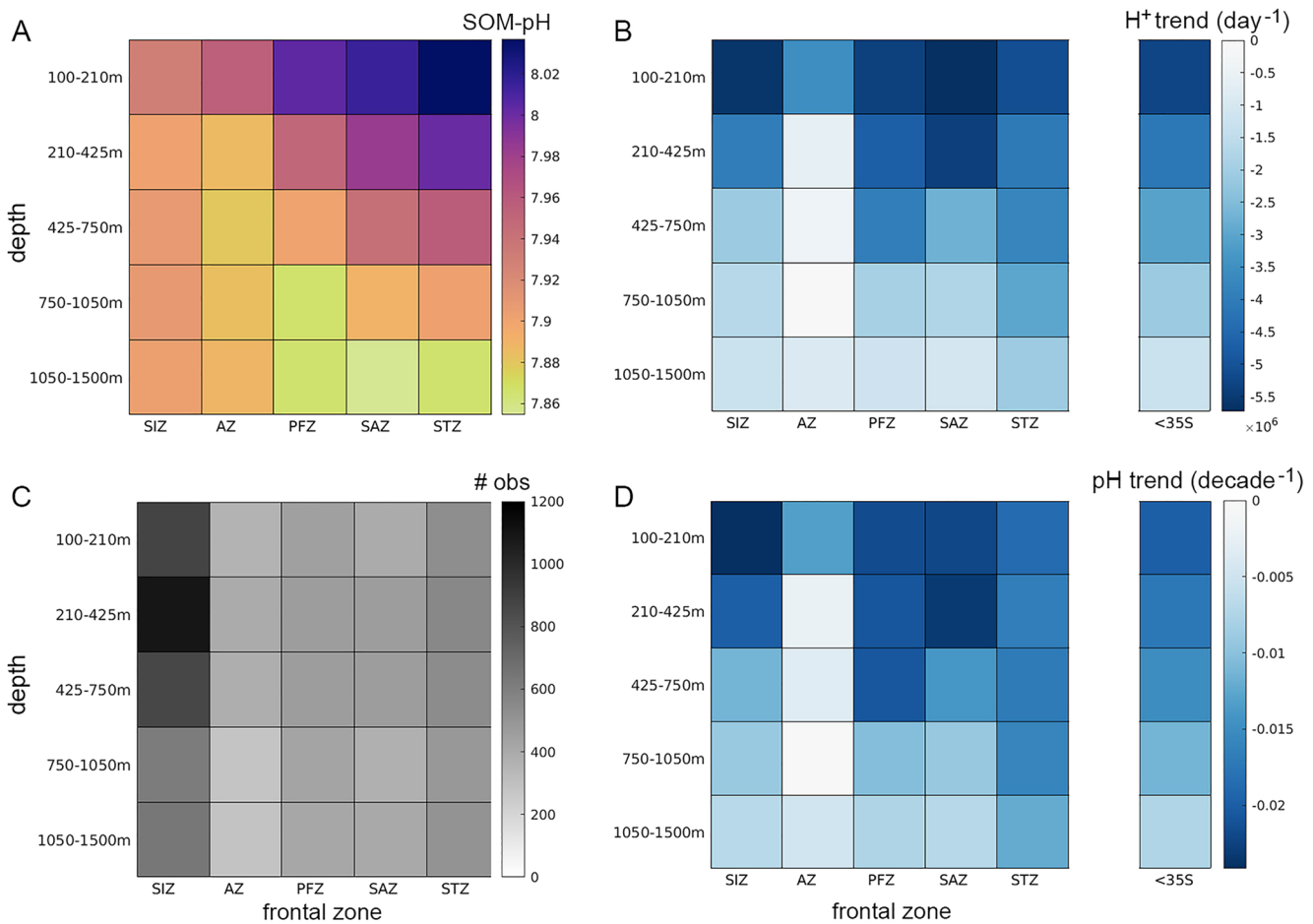

Figure 7. (a) The average Southern Ocean Carbon and Climate Observations and Modeling-era Objectively Mapped pH (SOM-pH) value in each depth bin and region. (b) H^+ trend (day^{-1}) of Global Ocean Data Analysis Project version 2 (GLODAPv2) observation differences to SOM-pH binned by depth and spatial region. (c) Number of GLODAPv2 observations in each depth and spatial region bin. (d) pH trend (decade^{-1}) of GLODAPv2 observation differences to SOM-pH. These pH trend values are also given in Table 2, showing that trends are all significantly different from zero except for the 750–1,050 m bin in the Antarctic Zone. The most poleward region, the Sea Ice Zone, is on the left, and the most equatorward region, the Subtropical Zone, is on the right.

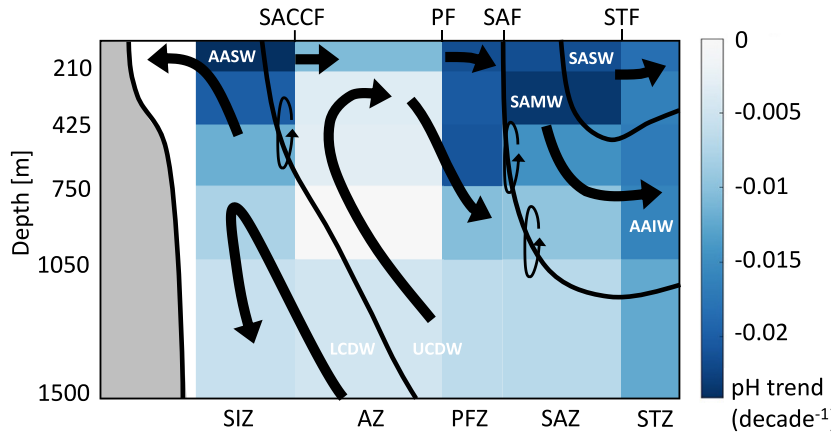

Figure 8. Trends from Figure 7d, but with a schematic of the Southern Ocean meridional overturning circulation superposed. This schematic is adapted from Talley (2011), and was originally published in Speer et al. (2000). Depth is on the *y*-axis, and the *x*-axis shows the regional zones of analysis, with the fronts separating them denoted at the top: Southern ACC Front (SACCF), Polar Front (PF), Subantarctic Front (SAF), and Subtropical Front (STF). Black lines denote the isopycnal slopes. Thick black arrows denote the overturning circulation, with eddies denoting diapycnal exchanges. Lower branch upwelling waters are labeled: Lower and Upper Circumpolar Deep Water (LCDW, UCDW). Once these waters upwell they are transformed via air–sea interaction into Antarctic Surface Water (AASW), Subantarctic Mode Water (SAMW), Antarctic Intermediate Water (AAIW), and Subantarctic Surface Water (SASW).

AAIW, and SASW. SAMW and AAIW are subducted to depth in the PFZ and SAZ, and then travel equatorward in the STZ. SASW is transported equatorward in the upper ocean. These waters show strong trends, implying that atmospheric exchange is dominating the trend signal, and sequestration of carbon by SAMW and AAIW is leading to strong pH trends in the intermediate ocean depths. Indeed, the strongest trends in the 750–1,500 m depth range occur in the STZ.

5. Discussion and Conclusions

The results presented here show a significant trend in pH in the Southern Ocean over the last 30 years. This trend has spatial structure consistent with the MOC. Old waters are being brought poleward and upwelling largely in the AZ. This AZ region has waters with less exposure to the surface high anthropogenic CO_2 signals, and indeed shows minimal trends at most depths. As these old waters approach the surface, some will move poleward in the SIZ and then recirculate or subduct. Thus it is not surprising to have strong trends in the upper 425 m of this SIZ region. Other waters reaching the surface in the AZ will move equatorward into the PFZ and SAZ and be subducted equatorward in the upper branch of the MOC. One may therefore expect the newly ventilated carbon rich waters to be found in the upper 750 m of the SAZ and into the STZ, and this is exactly what is observed. Old waters appear to be upwelled in the ACC, taking up increased CO_2 before subducting to the north. This is inferred by comparing the SOM-pH product with the raw GLODAPv2 data (Figure 7), and also with the GLODAPv2 mapped product (Figure 4): the strongest differences at 700 m occur in regions where one expects relatively recent ventilation by SAMW (Jones et al., 2016).

The spatial pattern of the pH trend points to air–sea carbon exchange as the causal mechanism. There are Southern Ocean regions that show net outgassing of carbon and regions that show net ingassing. We hypothesize that the outgassing is now weaker and ingassing now stronger due to anthropogenically driven increased atmospheric carbon levels. This is to be expected as ocean surface pCO_2 levels appear to be increasing by about 19 µatm per decade nearly uniformly across the world oceans, which is also approximately the rate of increase in mean atmospheric pCO_2 (Takahashi et al., 2014). Our hypothesis of the trend being anthropogenically surface forced is consistent with previous findings attributing surface pH trends of approximately 0.02 per decade along repeat hydrography lines in the South Pacific to the magnitude of the atmospheric pCO_2 trend (Williams et al., 2015). Moreover, inferred anthropogenic carbon changes along these hydrographic repeat lines show a similar pattern to the pH trends we find, with a reduced inventory in upwelling latitudes (Carter et al., 2018; Gruber et al., 2019). If the trends were primarily from internal ocean variability one would not necessarily expect the magnitudes to vary

so substantially across upwelling and downwelling regions of the Southern Ocean. Nevertheless, we cannot rule out that some of the trend structure may result from changing ocean circulation, and further attribution studies should be carried out. Comparing the pH trends with other property trends may better inform causal mechanisms.

The Southern Ocean is incredibly energetic, and internal ocean turbulence is so great that interannual variability in physical properties can be hard to detect over the shorter timescale variability. Indeed, detecting heating trends requires careful accounting for eddy variability (Gille, 2002), but is made possible due to a relatively large amount of temperature data. Earlier works have assessed pH trends by "matchup" or cross-over calculations. These include eddy noise in both components, and thus the results were less robust. By building a climatology for the SOCCOM-era we are giving a best estimate of the eddy-filtered current state. Yet given sparse sampling, we acknowledge that eddy variability can creep into our product. Nevertheless, the trends are clearly detectable above the uncertainty in pH due to their significant magnitude. We find that pH is decreasing by approximately 0.02 per decade over large regions, which is consistent with the previous match-up based works (Midorikawa et al., 2012; Ríos et al., 2015; Swart et al., 2018). With a typical pH dynamic range estimated at 0.2, this therefore represents a 10% change to pH each decade.

While useful, the schematic in Figure 8 is overly simplified. The Southern Ocean MOC follows a complicated three-dimensional path (Tamsitt et al., 2017). Because data are too sparse to sort by longitude, as can be seen in Figure 5 where all profiles taken before 2009 are shown, we have chosen to sort only by depth and meridional region for this paper. Thus a caveat of this work is that we may be aliasing this zonal structure into our interpretation of the relationship of acidification with the MOC. Assessing trends along density surfaces may help account for the influences of both eddy and zonal structures. However, the thickness of the bins and the zonal structure in our meridional regions are an attempt to mitigate these issues, and we leave more targeted efforts to understand the full structure of pH changes to future studies.

The SOM-pH product is made available as Data Set S1. We anticipate future updates to this product as the BGC-Argo array continues to provide vital observations of ocean health. We also plan to apply this mapping methodology to other BGC-Argo observation, including nitrate and oxygen. We hope this SOM-pH BGC-Argo map will be useful for understanding the changing Southern Ocean properties and ecosystems.

Data Availability Statement

SOM-pH is available at http://sose.ucsd.edu/CLIM/PH-QCv3-v10r1.nc and as Data Set S1 provided with this manuscript. Argo data (Argo, 2020) were collected and made freely available by the International Argo Program and the national programs that contribute to it (http://www.argo.ucsd.edu, http://argo.jcommops.org). The Argo Program is part of the Global Ocean Observing System (http://doi.org/10.17882/42182).

Acknowledgments
Information on accessing data presented is given in the following Data Availability Statement section. This work is a contribution of the SOCCOM project, which is supported under NSF Award PLR-1425989 and OPP-1936222. In addition, Mazloff acknowledges support from NSF Awards OCE-1924388 and OPP-2149501 and NOPP award NA19OAR4310361. We acknowledge Joellen Russell for providing computing resources at the University of Arizona enabling the construction of the SOM-pH product. This paper benefited from conversations with Brendan Carter and feedback from two anonymous reviewers.

References

Argo. (2020). Argo float data and metadata from global data assembly centre (Argo GDAC) [Dataset]. https://doi.org/10.17882/42182

Bittig, H. C., Steinhoff, T., Claustre, H., Fiedler, B., Williams, N. L., Sauzede, R., et al. (2018). An alternative to static climatologies: Robust estimation of open ocean CO_2 variables and nutrient concentrations from T, S, and O_2 data using Bayesian neural networks. *Frontiers in Marine Science*, *5*, 328. https://doi.org/10.3389/fmars.2018.00328

Bretherton, F. P., Davis, R. E., & Fandry, C. (1976). A technique for objective analysis and design of oceanographic experiments applied to MODE-73. *Deep-Sea Research and Oceanographic Abstracts*, *23*(7), 559–582. https://doi.org/10.1016/0011-7471(76)90001-2

Carter, B. R., Feely, R. A., Williams, N. L., Dickson, A. G., Fong, M. B., & Takeshita, Y. (2018). Updated methods for global locally interpolated estimation of alkalinity, pH, and nitrate. *Limnology and Oceanography: Methods*, *16*(2), 119–131. https://doi.org/10.1002/lom3.10232

Doney, S. C., Busch, D. S., Cooley, S. R., & Kroeker, K. J. (2020). The impacts of ocean acidification on marine ecosystems and reliant human communities. *Annual Review of Environment and Resources*, *45*(1), 83–112. https://doi.org/10.1146/annurev-environ-012320-083019

Doney, S. C., Fabry, V. J., Feely, R. A., & Kleypas, J. A. (2009). Ocean acidification: The other CO_2 problem. *Annual Review of Marine Science*, *1*, 169–192. https://doi.org/10.1146/annurev.marine.010908.163834

Fassbender, A. J., Orr, J. C., & Dickson, A. G. (2021). Interpreting pH changes. *Biogeosciences*, *18*(4), 1407–1415. https://doi.org/10.5194/bg-18-1407-2021

Galbraith, E. D., Gnanadesikan, A., Dunne, J. P., & Hiscock, M. R. (2010). Regional impacts of iron-light colimitation in a global biogeochemical model. *Biogeosciences*, *7*(3), 1043–1064. https://doi.org/10.5194/bg-7-1043-2010

Gaspari, G., & Cohn, S. E. (1999). Construction of correlation functions in two and three dimensions. *Quarterly Journal of the Royal Meteorological Society*, *125*(554), 723–757. https://doi.org/10.1002/qj.49712555417

Gille, S. T. (2002). Warming of the Southern Ocean since the 1950s. *Science*, *295*(5558), 1275–1277. https://doi.org/10.1126/science.1065863

Gray, A. R., Johnson, K. S., Bushinsky, S. M., Riser, S. C., Russell, J. L., Talley, L. D., et al. (2018). Autonomous biogeochemical floats detect significant carbon dioxide outgassing in the high-latitude Southern Ocean. *Geophysical Research Letters*, *45*(17), 9049–9057. https://doi.org/10.1029/2018gl078013

Gruber, N., Clement, D., Carter, B. R., Feely, R. A., van Heuven, S., Hoppema, M., et al. (2019). The oceanic sink for anthropogenic CO_2 from 1994 to 2007. *Science*, *363*(6432), 1193–1199. https://doi.org/10.1126/science.aau5153

Henley, S. F., Cavan, E. L., Fawcett, S. E., Kerr, R., Monteiro, T., Sherell, R. M., et al. (2020). Changing biogeochemistry of the Southern Ocean and its ecosystem implications. *Frontiers in Marine Science*, *7*, 81. https://doi.org/10.3389/fmars.2020.00581

Ide, K., Courtier, P., Ghil, M., & Lorenc, A. C. (1997). Unified notation for data assimilation: Operational, sequential and variational (special issue data assimilation in meteology and oceanography: Theory and practice). *Journal of the Meteorological Society of Japan. Ser. II*, *75*(1B), 181–189. https://doi.org/10.2151/jmsj1965.75.1B_181

Johnson, G. C., Hosoda, S., Jayne, S. R., Oke, P. R., Riser, S. C., Roemmich, D., et al. (2022). Argo-two decades: Global oceanography, revolutionized. *Annual Review of Marine Science*, *14*(1), 379–403. https://doi.org/10.1146/annurev-marine-022521-102008

Johnson, K. S., Jannasch, H. W., Coletti, L. J., Elrod, V. A., Martz, T. R., Takeshita, Y., et al. (2016). Deep-Sea DuraFET: A pressure tolerant pH sensor designed for global sensor networks. *Analytical Chemistry*, *88*(6), 3249–3256. https://doi.org/10.1021/acs.analchem.5b04653

Johnson, K. S., Plant, J. N., Coletti, L. J., Jannasch, H. W., Sakamoto, C. M., Riser, S. C., et al. (2017). Biogeochemical sensor performance in the SOCCOM profiling float array. *Journal of Geophysical Research: Oceans*, *122*(8), 6416–6436. https://doi.org/10.1002/2017jc012838

Jones, D. C., Meijers, A. J., Shuckburgh, E., Sallée, J.-B., Haynes, P., Mcaufield, E. K., & Mazloff, M. R. (2016). How does Subantarctic Mode Water ventilate the Southern Hemisphere subtropics? *Journal of Geophysical Research: Oceans*, *121*(9), 6558–6582. https://doi.org/10.1002/2016jc011680

Key, R., Olsen, A., van Heuven, S., Lauvset, S. K., Velo, A., Lin, X., et al. (2015). *Global Ocean data analysis project, version 2 (GLODAPv2)*. ORNL/CDIAC-162, ND-P093, Carbon Dioxide Inf. Anal. Cent., Oak Ridge Natl. Lab., U.S. Dep. of Energy, Oak Ridge, Tenn. https://doi.org/10.3334/CDIAC/OTG.NDP093_GLODAPv2

Lauvset, S. K., Key, R. M., Olsen, A., van Heuven, S., Velo, A., Lin, X., et al. (2016). A new global interior ocean mapped climatology: The $1° \times 1°$ GLODAP version 2. *Earth System Science Data*, *8*(2), 325–340. https://doi.org/10.5194/essd-8-325-2016

Liu, X., Patsavas, M. C., & Byrne, R. H. (2011). Purification and characterization of meta-Cresol purple for spectrophotometric seawater pH measurements. *Environmental Science & Technology*, *45*(11), 4862–4868. https://doi.org/10.1021/es200665d

Marshall, J., & Speer, K. (2012). Closure of the meridional overturning circulation through Southern Ocean upwelling. *Nature Geoscience*, *5*(3), 171–180. https://doi.org/10.1038/ngeo1391

Maurer, T. L., Plant, J. N., & Johnson, K. S. (2021). Delayed-mode quality control of oxygen, nitrate, and pH data on SOCCOM biogeochemical profiling floats. *Frontiers in Marine Science*, *8*, 683207. https://doi.org/10.3389/fmars.2021.683207

McNeil, B. I., & Matear, R. J. (2008). Southern Ocean acidification: A tipping point at 450-ppm atmospheric CO_2. *Proceedings of the National Academy of Sciences of the United States of America*, *105*(48), 18860–18864. https://doi.org/10.1073/pnas.0806318105

Midorikawa, T., Inoue, H. Y., Ishii, M., Sasano, D., Kosugi, N., Hashida, G., et al. (2012). Decreasing pH trend estimated from 35-year time series of carbonate parameters in the Pacific sector of the Southern Ocean in summer. *Deep Sea Research Part I: Oceanographic Research Papers*, *61*, 131–139. https://doi.org/10.1016/j.dsr.2011.12.003

Munro, D. R., Lovenduski, N. S., Takahashi, T., Stephens, B. B., Newberger, T., & Sweeney, C. (2015). Recent evidence for a strengthening CO_2 sink in the Southern Ocean from carbonate system measurements in the Drake Passage (2002–2015). *Geophysical Research Letters*, *42*(18), 7623–7630. https://doi.org/10.1002/2015GL065194

Olsen, A., Key, R. M., van Heuven, S., Lauvset, S. K., Velo, A., Lin, X., et al. (2016). The global ocean data analysis project version 2 (GLODAPv2)–an internally consistent data product for the world ocean. *Earth System Science Data*, *8*(1), 297–323. https://doi.org/10.5194/essd-8-297-2016

Olsen, A., Lange, N., Key, R. M., Tanhua, T., Álvarez, M., Becker, S., et al. (2019). GLODAPv2. 2019–an update of GLODAPv2. *Earth System Science Data*, *11*(3), 1437–1461. https://doi.org/10.5194/essd-11-1437-2019

Orr, J. C., Fabry, V. J., Aumont, O., Bopp, L., Doney, S. C., Feely, R. A., et al. (2005). Anthropogenic ocean acidification over the twenty-first century and its impact on calcifying organisms. *Nature*, *437*(7059), 681–686. https://doi.org/10.1038/nature04095

Orsi, A. H., Whitworth, T., & Nowlin, W. D. (1995). On the meridional extent and fronts of the Antarctic Circumpolar Current. *Deep Sea Research Part I: Oceanographic Research Papers*, *42*(5), 641–673. https://doi.org/10.1016/0967-0637(95)00021-W

Ríos, A. F., Resplandy, L., García-Ibáñez, M. I., Fajar, N. M., Velo, A., Padin, X. A., et al. (2015). Decadal acidification in the water masses of the Atlantic Ocean. *Proceedings of the National Academy of Sciences of the United States of America*, *112*(32), 9950–9955. https://doi.org/10.1073/pnas.1504613112

Riser, S. C., Swift, D., & Drucker, R. (2018). Profiling floats in SOCCOM: Technical capabilities for studying the Southern Ocean. *Journal of Geophysical Research: Oceans*, *123*(6), 4055–4073. https://doi.org/10.1002/2017jc013419

Roemmich, D., & Gilson, J. (2009). The 2004–2008 mean and annual cycle of temperature, salinity, and steric height in the global ocean from the Argo Program. *Progress in Oceanography*, *82*(2), 81–100. https://doi.org/10.1016/j.pocean.2009.03.004

Speer, K., Rintoul, S. R., & Sloyan, B. (2000). The diabatic Deacon cell. *Journal of Physical Oceanography*, *30*(12), 3212–3222. https://doi.org/10.1175/1520-0485(2000)030<3212:tddc>2.0.co;2

Swart, S., Johnson, K., Mazloff, M. R., Meijers, A., Meredith, M., Newman, L., & Sallee, J.-B. (2018). Southern Ocean [in "State of the Climate in 2017"]. *Bulletin of the American Meteorological Society*, *99*(8), S307–S309. https://doi.org/10.1175/BAMS-D-20-0090.1

Takahashi, T., Sutherland, S., Chipman, D., Goddard, J., Ho, C., Newberger, T., et al. (2014). Climatological distributions of pH, pCO_2, total CO_2, alkalinity, and $CaCO_3$ saturation in the global surface ocean, and temporal changes at selected locations. *Marine Chemistry*, *164*, 95–125. https://doi.org/10.1016/j.marchem.2014.06.004

Talley, L. D. (2011). *Descriptive physical oceanography: An introduction*. Academic Press.

Tamsitt, V., Drake, H. F., Morrison, A. K., Talley, L. D., Dufour, C. O., Gray, A. R., et al. (2017). Spiraling pathways of global deep waters to the surface of the Southern Ocean. *Nature Communications*, *8*(1), 1–10. https://doi.org/10.1038/s41467-017-00197-0

Verdy, A., & Mazloff, M. R. (2017). A data assimilating model for estimating Southern Ocean biogeochemistry. *Journal of Geophysical Research: Oceans*, *122*(9), 6968–6988. https://doi.org/10.1002/2016jc012650

Williams, N. L., Feely, R. A., Sabine, C. L., Dickson, A. G., Swift, J. H., Talley, L. D., & Russell, J. L. (2015). Quantifying anthropogenic carbon inventory changes in the Pacific sector of the Southern Ocean. *Marine Chemistry*, *174*, 147–160. https://doi.org/10.1016/j.marchem.2015.06.015

Wunsch, C. (2006). *Discrete inverse and state estimation problems: With geophysical fluid applications*. Cambridge University Press.

Wunsch, C., & Heimbach, P. (2008). How long to oceanic tracer and proxy equilibrium? *Quaternary Science Reviews*, *27*(7), 637–651. https://doi.org/10.1016/j.quascirev.2008.01.006

Wunsch, C., & Heimbach, P. (2013). Chapter 21 - Dynamically and kinematically consistent global ocean circulation and ice state estimates. In G. Siedler, S. M. Griffies, J. Gould, & J. A. Church (Eds.), *Ocean circulation and climate a 21st century perspective* (Vol. 103, pp. 553–579). Academic Press. https://doi.org/10.1016/B978-0-12-391851-2.00021-0

Yao, W., Liu, X., & Byrne, R. H. (2007). Impurities in indicators used for spectrophotometric seawater pH measurements: Assessment and remedies. *Marine Chemistry*, *107*(2), 167–172. https://doi.org/10.1016/j.marchem.2007.06.012